Aerospace Science and Technology 159 (2025) 110017

Contents lists available at ScienceDirect

Aerospace Science and Technology

journal homepage: www.elsevier.com/locate/aescte

Suppression of flow separation of a high-lift wing with active flow control

Qiangqiang Sun [a], Faycal Bahri [a], Mark Jabbal [a,*], Wit Stryczniewicz [b], Richard Jefferson-Loveday [c,*], Bruno Stefes [d], Alexander Büscher [d]

[a] Faculty of Engineering, University of Nottingham, Nottingham, NG7 2RD, UK
[b] Aerodynamics Department, Łukasiewicz Research Network—Institute of Aviation, Al. Krakowska 110/114, 02-256, Warszawa, Poland
[c] Faculty of Natural, Mathematical & Engineering Sciences, King's College London, London, WC2R 2LS, UK
[d] Airbus Operations GmbH, Airbus-Allee 1, Bremen, 28199, Germany

ARTICLE INFO

Communicated by Damiano Casalino

Keywords:
Lift enhancement
Flow separation
Multi-element wing
Active flow control
Pulsed jet flow control

ABSTRACT

Flow separation caused by the integration of a leading edge slat cut-out to accommodate an ultra-high bypass ratio engine reduces the maximum lift coefficient. In this study, an active flow control approach including 88 pulsed jet nozzles near the leading edge is used to control flow separation over a multi-element high-lift aerofoil. A hybrid large-eddy simulation (LES) and stress-blended eddy simulation (SBES) method is deployed to analyze flow physics and wind tunnel tests are also performed for the flow with/without control. The results show that severe flow separation is observed for the clean case by visualizing the streamlines on the airfoil's surface via numerical and experimental methods. Compared with the clean case, the stall angle is delayed by around 4°, and the maximum lift coefficient is increased by more than 15% after deploying the active flow control. Meanwhile, when the active flow control is imposed, a lift enhancement region caused by the vortex shedding downstream of the jet nozzles is formed adjacent to the leading edge, and its scale becomes larger along the spanwise direction.

1. Introduction

Aerofoil performance in aircraft operations including runway distance, climb rate, operational range, and payload capacity, is crucial [1]. To ensure enough lift at low flight speed during landing and take-off operations, high-lift devices including leading edge and trailing edge devices are employed to increase the lift coefficient. Generally, high-lift devices include a single slat (near the leading edge) and a single flap (near the trailing edge). Meanwhile, modern airplanes often have large slat cut-outs due to the growth in engine diameter. Then, the result of the cut-out is that the downstream flow field is contaminated by the additional vortices generated at the interfacial cut-out corners between the slat and the main element. These vortices strongly influence the flow behaviour of the airfoil by triggering flow separation, which can lead to loss of the available lift and even wing stall [2].

Therefore, various methods are actively explored to overcome the degradation of the airplane wing performance caused by flow separation [3–5]. For example, Jirasek et al. [6] showed that vortex generators as passive control devices are effective for suppressing flow separation under some conditions. However, these vortex generators usually cause a drag penalty when the flow does not separate. On the other hand, the active jet control system has been proven as an effective technique in suppressing flow separation owing to the fact that jet flow can stabilize the boundary layer flow by adding/removing momentum to/from the boundary layer and forming vortical structures [7–10]. The vortical structures also enhance the boundary layer flow mixing and momentum exchange between the inner and outer parts of the boundary layer. Hue et al. [2] numerically investigated the effects of constant blowing devices with different slot sizes, types and injection velocities on the characteristics of an aircraft in a high-lift configuration, and found that the lift coefficient was enhanced by ~ 3% and the stall angle was delayed around one to two degrees.

According to previous efforts [11–14], the control performance of dynamic blowing is superior to constant blowing due to the enhanced vorticity production associated with the former approach [15]. As an important parameter of the dynamic flow control, the optimum actuation frequency f is usually chosen in the same order as the shedding frequency of the dominant eddy f_s in the shear layer, namely, $\mathcal{O}(f/f_s) \approx 1$

* Corresponding author.
E-mail addresses: ezzmj@exmail.nottingham.ac.uk (M. Jabbal), richard.jefferson-loveday@kcl.ac.uk (R. Jefferson-Loveday).

https://doi.org/10.1016/j.ast.2025.110017
Received 17 November 2024; Received in revised form 30 January 2025; Accepted 3 February 2025

Available online 5 February 2025

Nomenclature

α, α_1	angle of attack ..... °	μ	dynamic viscosity ..... $Pa \cdot s$
C	chord length ..... m	p, p_∞ or p'	pressure, freestream pressure, or fluctuation pressure ..... Pa
C_l	lift coefficient	τ	stress tensor ..... Pa
C_d	drag coefficient	S	strain rate tensor ..... s^{-1}
C_p	pressure coefficient, $C_p = (p - p_\infty)/(0.5\rho_\infty U_\infty^2)$	t	time ..... s
C_{pt}	total pressure coefficient, $C_{pt} = (p + 0.5\rho U^2 - p_\infty)/(0.5\rho_\infty U_\infty^2)$	T_{jet}	pulsed jet flow period, $0.02\,s$
		T_c	convective time scale, $T_c = C/U_c$ ..... s
U or U_∞	velocity or freestream velocity ..... m/s	Δt^*	dimensionless time step, $\Delta t^* = t/(C/U_\infty)$
U_c	convective velocity, $U_c = U_\infty cos(28°)$ ..... m/s	τ_w	wall shear stress ..... Pa
U_{jet} or $U_{jet,max}$	jet flow velocity or maximum jet flow velocity m/s	x, y, z	coordinate ..... m
DC	duty circle	Δz	cross-stream grid spacing ..... m
f	actuation frequency, 50 Hz	Δx^+	wall unit in the x direction
f_s	dominant vortex shedding frequency	Δy^+	wall unit in the y direction
F^+	dimensionless actuation frequency, $F^+ = fC/U_\infty$	Δz^+	wall unit in the z direction
ρ	or ρ_∞] density or freestream density ..... Kg/m^3		

[16,17]. This is based on two observations [18]: (1) acoustic excitation experiments show a trend toward the aforementioned criterion when the forcing intensity is increased [19]; (2) it was shown that the expansion rate of a turbulent free shear layer can be enhanced most effectively through excitation with such a frequency [20,21]. Therefore, the primary objective of the present study is to numerically investigate and further reveal physical mechanisms of flow separation suppression achieved by dynamic blowing with such an optimum actuation frequency, which can complement previous experimental studies. Another objective is to analyze the lift enhancement mechanisms caused by the pulsed active flow approach, which has not been actively explored before.

However, the accurate prediction of the lift coefficient by conducting numerical simulations is a challenging task because of the geometric complexities of the airfoil and high-lift systems [22,23]. Meanwhile, the flow over an airfoil involves strong and complex nonlinear interactions between the viscous and inviscid flow features. It also presents various complex physical phenomena such as flow separation, the confluence of boundary layers and wakes and strong pressure gradients [24]. For the prediction of such unsteady flow, large-eddy simulation (LES) instead of the traditional computational fluid dynamics (CFD) techniques based on the well-known Reynolds-averaged Navier-Stokes (RANS) equations are extensively employed [23,25,26]. This is because the three-dimensional smooth body flow separation of a high-lift configuration cannot be reliably predicted by the steady RANS or URANS models, irrespective of the turbulence model [23,27–29]. However, the LES method presents detailed temporal and spatial information regarding a wide range of turbulence scales [24,30]. Based on the comment of reference [23,31], however, LES is unlikely to be used in aircraft design until around 2045 due to the expense. An intermediate step is to employ hybrid RANS/LES methods, in which the attached and separated boundary layers are simulated using an underlying RANS turbulence model and an LES-like scale-resolving strategy, respectively [23].

In this study, therefore, numerical simulations are performed by using a hybrid model combining the LES and stress-blended eddy simulation (SBES) to investigate the flow separation control of a multi-element high-lift airfoil with and without the active flow control devices, and to understand the underpinning physics mechanism of the suppression of flow separation. The numerical results are compared with experimental measurements of the same configuration. The numerical simulation details and experimental configurations are introduced in Sec. 2. The corresponding results including flow separation suppression and lift coefficient enhancement mechanisms are presented and discussed in Sec. 3. Finally, the main conclusions of this work are drawn in Sec. 4.

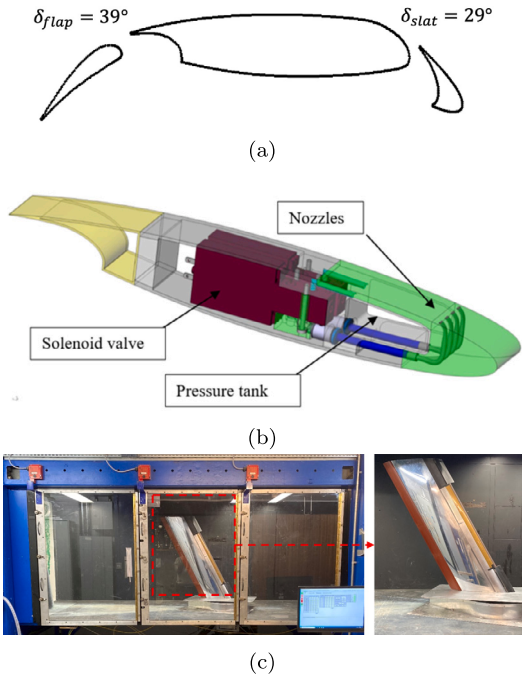

Fig. 1. (a) Landing configuration of the DLR-F15 airfoil. (b) View of the active flow control system, and this figure is reprinted from reference [32]. (c) Experimental setup with DLR-F15 inside the wind tunnel.

2. Experimental and numerical methodology

2.1. Experimental details

Fig. 1a shows the DLR-F15 model investigated in this work. The deflection angles for the slat and flap are 29°and 39°, respectively. The chord length C is $0.34\,m$, and the length of the airfoil in the spanwise direction is $3.90\,C$. The lengths of the slat and flap are $0.15\,C$ and $0.30\,C$, respectively. The sweep angle is 28°. The wing model is a state-of-the-art concept manufactured by Institute of Aviation (ILOT) [32]. The actuators are employed on the suction side of the leading edge of the main element to suppress the local flow separation. The experimental actuation system consists of three major components: a pressurized air supply, fast switching solenoid valves to generate pulsed airflow, and actuator chambers, as shown in Fig. 1b. The jet enters the ambient flow through an orifice in the main element's surface as a fast pulsed jet. A total of 88 rectangular jets near the leading edge are distributed equally along

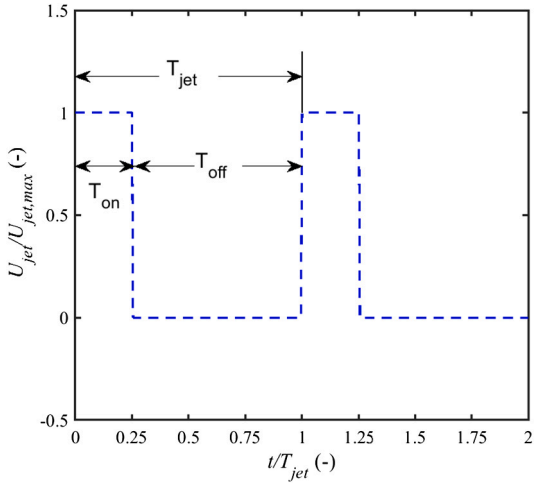

Fig. 2. Unsteady blowing boundary conditions applied in experiments and simulations.

the slat cut-out region. The distance between each nozzle and the leading edge is $0.13C$. Each jet nozzle has a spanwise length of $3.5 \times 10^{-3}\, m$ and a chordwise length of $0.7 \times 10^{-3}\, m$. The distance between each two nozzles is $3.5 \times 10^{-3}\, m$. All jets are operated through 44 solenoid valves, and each valve feeds two adjacent jets. The valves are individually controlled in frequency and duty cycle, and they are connected to a pressure tank embedded inside the model. Pressure, temperature and mass flow rate are constantly monitored at the inlet of the tank during the experiment. Furthermore, the model is equipped with a centreline row of 64 static pressure taps dedicated to measuring the pressure distribution along the upper and lower sides of the main body and the flap. Fig. 1c shows the experimental setup including the DLR-F15 mounted inside the wind tunnel.

For all cases reported in the following sections, the values of the freestream velocity U_∞ and maximum jet flow control velocity $U_{jet,max}$ are $30\, m/s$ and $100\, m/s$, respectively. The Reynolds number is 6.93×10^5. There are no trips attached to the leading edge, and the transition of laminar inflow to turbulent flow occurs naturally. To ensure that the actuation frequency is in the same order as the shedding frequency of the largest eddy in the shear layer shown in Fig. 3, the dimensionless actuation frequency is chosen as $F^+ = fC/U_\infty = 0.56$, where f is $50\, Hz$. Such a frequency response of the experimental actuators can be achieved, as presented in our partner's work [32]. In addition, the duty circle (DC) is configured as $DC = 25\%$.

2.2. Simulation details

2.2.1. Governing equations

The turbulent flow over the multi-element wing is governed by the Navier-Stokes equations used in reference [33]

$$\frac{\partial \tilde{\rho}}{\partial t} + \frac{\partial}{\partial x_i}\left(\tilde{\rho}\tilde{U}_i\right) = 0, \tag{1a}$$

$$\frac{\partial}{\partial t}\left(\tilde{\rho}\tilde{U}_i\right) + \frac{\partial}{\partial x_j}\left(\tilde{\rho}\tilde{U}_i\tilde{U}_j\right) = -\frac{\partial \tilde{p}}{\partial x_i} + \frac{\partial \tilde{\tau}_{ij}}{\partial x_j}, \tag{1b}$$

where $\tilde{U}_i$ is the velocity in the i ($i = 1, 2, 3$) direction, x is the coordinate, t is the time, $\tilde{p}$ is the pressure and $\tilde{\rho}$ is the density. In this work, the tilde and "T" subscript are used to show that each variable has dual meanings [33]. Namely, in a RANS simulation, the tilde denotes an ensemble averaging operation. However, it represents a spatially filtered variable, and $\mu_T = \mu_{sgs}$ (the sub-grid scale viscosity) for LES simulation. The Smagorinsky closure [33,34] is adopted for the hybrid LES-SBES model [35] in this work.

The stress tensor $\tilde{\tau}_{ij}$ is computed using

$$\tilde{\tau}_{ij} = 2(\mu + \mu_T)\left(\tilde{S}_{ij} - \frac{1}{3}\frac{\partial \tilde{U}_j}{\partial x_j}\delta_{ij}\right), \tag{2}$$

where μ is the dynamic viscosity, and δ_{ij} is the Kronecker delta function ($\delta_{ij} = 1$ if $i = j$ and $\delta_{ij} = 0$ if $i \neq j$). The strain rate tensor $\tilde{S}_{ij}$ is expressed as

$$\tilde{S}_{ij} = \frac{1}{2}\left(\frac{\partial \tilde{U}_i}{\partial x_j} + \frac{\partial \tilde{U}_j}{\partial x_i}\right). \tag{3}$$

The Dirichlet boundary conditions are applied for the inlet of the computational domain and jet flow nozzles. One should note that the velocity of the jet flow is a time-dependent signal, as shown in Fig. 2. For the outlet of the computational domain, the pressure boundary condition is employed. The no-slip wall boundary condition is configured for all airfoil surfaces. The non-dimensional time step Δt^* is 0.0015. In terms of the numerical schemes, the temporal integration method employed to solve the governing equation is based on the second-order implicit approach [36]. The pressure-velocity coupling is achieved by the SIMPLEC scheme. The turbulence and momentum terms are discretized by the second-order upwind scheme and central-differencing scheme, respectively.

2.2.2. The mesh generation

The wing model in numerical simulations is shown in Fig. 4. The computational domain has a shape of a cuboid, and the high-lift multi-element airfoil is fixed in it. The cuboid has a length of $12C$ with $2C$ upstream in the streamwise direction and $4C$ in the crossflow direction. To capture the near-wall flow-aligned streak-like structures and flow separation phenomenon, a fine cross-stream mesh spacing is required. As pointed out by Tucker et al. [37], the cross-stream mesh spacing of almost 20 wall units (namely, $\Delta z^+ = \Delta z\sqrt{\tilde{\rho}\tau_w}/\mu \approx 20$, where Δz is the cross-stream grid spacing, τ_w is the wall shear stress and μ is the dynamic viscosity of the fluid) is required to obtain an adequate streak resolution. Similarly, a streamwise (x direction) mesh spacing of almost 100 wall units (namely, $\Delta x^+ \approx 100$) is also needed to perform a wall-resolved LES. For our wing model, the total number of mesh cells will be more than 1.5 billion if we strictly follow the aforementioned meshing rules and employ the LES approach to investigate the active flow control achieved by the jet flow. This extremely large mesh count poses a challenge to computational resources and data storage. Fortunately, Davidson et al. [38] proposed the zonal modelling approach and reported that a significant enhancement of the cross-stream grid spacing ($100 \leq \Delta z^+ \leq 300$) is possible for the zonal LES turbulence model. In this study, the jet flow nozzles are located on the leading edge and we are interested in active flow control for the middle part of the high-lift multi-element airfoil. Therefore, a hybrid LES-SBES approach [35] is employed for balancing the computational accuracy and expense. As shown in Fig. 4, the middle part and the two end sections of the airfoil are modelled by the LES and SBES models, respectively.

Fully structured mesh points are generated for the high-lift airfoil. All wall surfaces are wrapped by a thin O-type block to ensure grid orthogonality [39]. Similar to previous efforts [24,39–41], the non-uniform mesh is generated after balancing the computational accuracy and resources. The boundary layer region is modelled using 30 hexagonal mesh layers and the wall-normal spacing of the first layer of the structured mesh is carefully chosen to ensure $\Delta y^+ \leq 1$, and each nozzle is discretized with around 70 mesh nodes. The total number of mesh cells is around 70 million. The values of Δx^+, Δy^+ and Δz^+ meet the aforementioned meshing rules suggested by Tucker [37] and Davidson et al. [38].

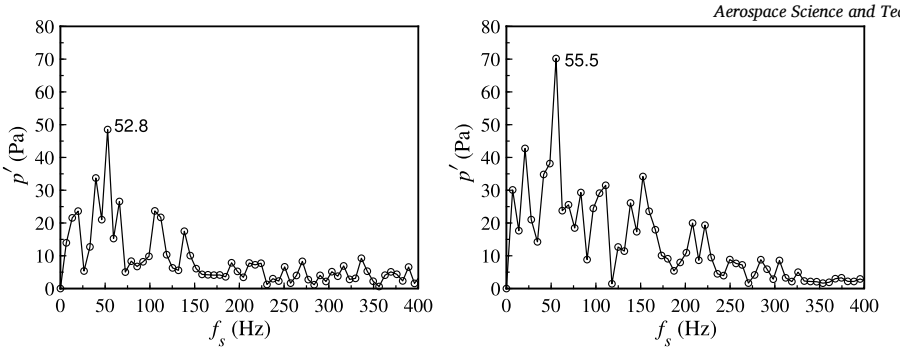

(a) A $(0.55C, 0.13C, 1.42C)$ (b) B $(0.64C, 0.23C, 1.42C)$

Fig. 3. Profiles of pressure fluctuation frequency of two random monitor points in the shear layer. The results are obtained from numerical simulations of the clean case.

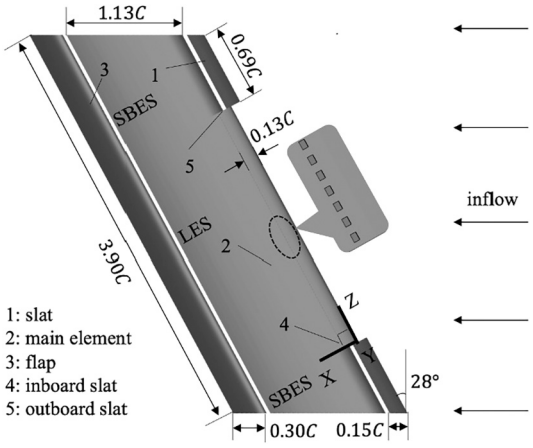

Fig. 4. Numerical models of the high-lift multi-element airfoil.

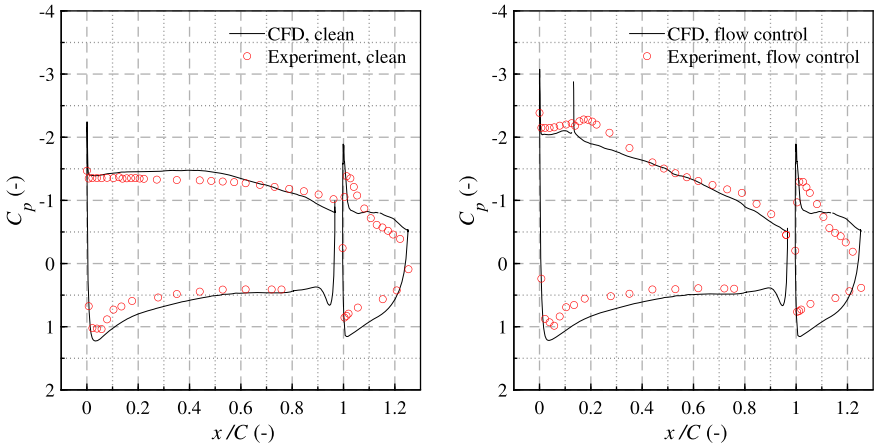

(a) Clean case (b) Active flow control case

Fig. 5. Comparison of the pressure coefficients obtained from simulations and experiments at the cut plane of $z/C = 1.42$ at $\alpha = \alpha_1$.

3. Computational and experimental results

3.1. Validation

Before investigating the active flow control, it is meaningful to conduct computations and experiments on the airfoil without any control system which is referred as the clean case throughout this work. This can be considered as a reference to verify the effectiveness of the deployed control technique. The time-averaged pressure coefficient at the cut-plane of $z/C = 1.42$ obtained from experiment and numerical simulation is compared in Fig. 5. It should be noted that the pressure coefficient refers to the static one throughout this work unless otherwise specified. For the clean and control cases, pressure coefficients of the main element (namely, $0 \leq x/C < 1$) computed by two methods are in good agreement with each other, and the agreement is comparable to the agreement reported in reference [42,43]. A slightly larger difference is observed for the flap ($1 \leq x/c \leq 1.25$), which is responsible for the gap of the lift coefficient shown in Fig. 7a.

The profiles of three dimensional streamlines at $\alpha = 0^{\circ}$and $\alpha = \alpha_1$ defined in Fig. 7 are presented in Fig. 6. The three dimensional separated

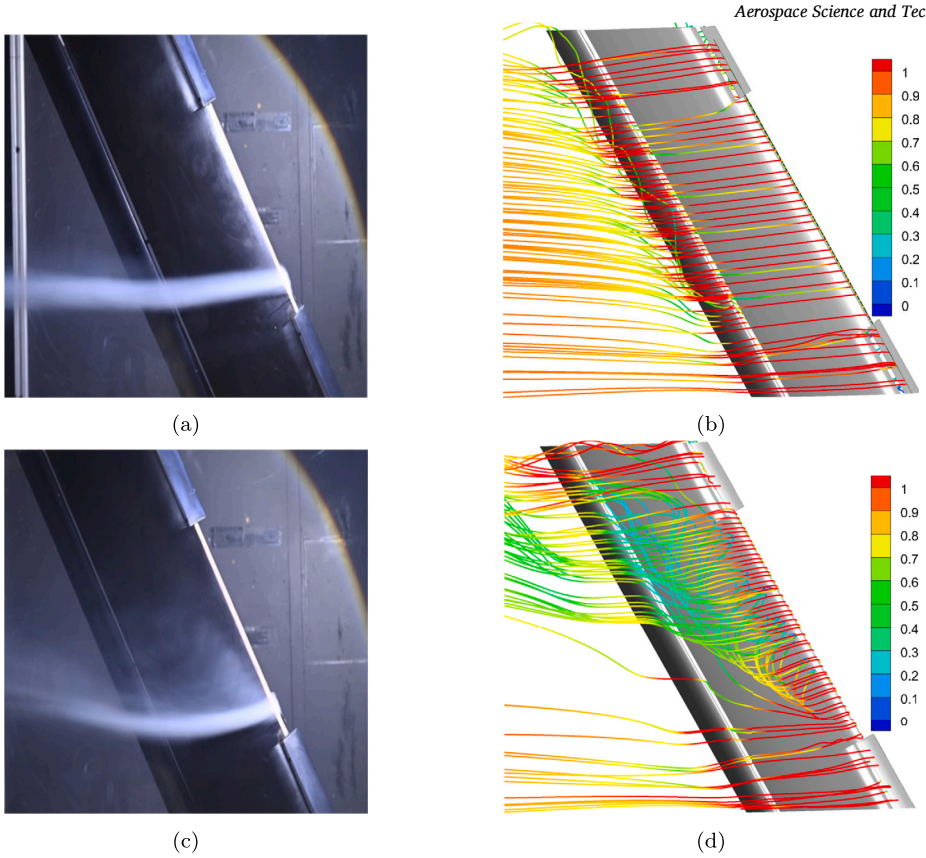

Fig. 6. The profiles of streamlines of the clean case. (a) $\alpha = 0°$, experiment, (b) $\alpha = 0°$, CFD, (c) $\alpha = \alpha_1$, experiment, (d) $\alpha = \alpha_1$, CFD. The CFD results are coloured by the dimensionless velocity magnitude.

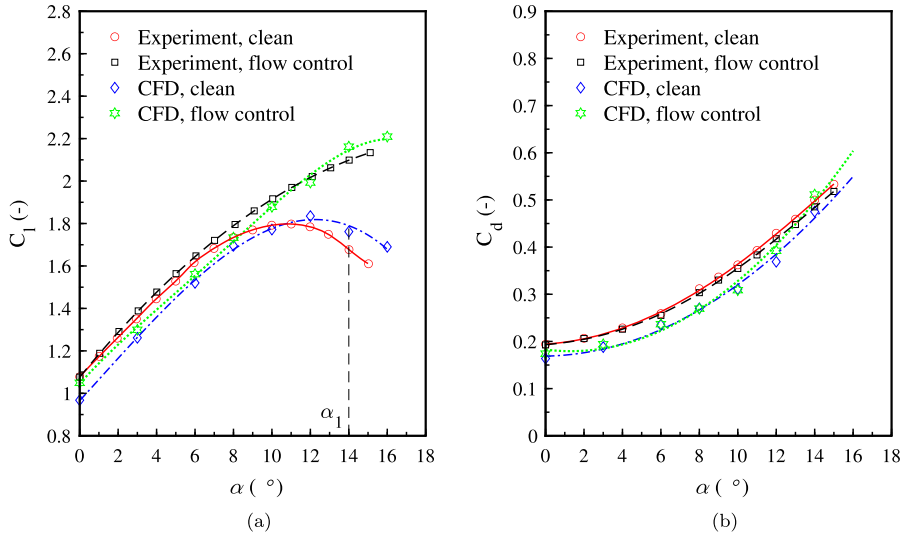

Fig. 7. (a) Lift and (b) drag coefficients at various angles of attack.

flow is visualized using the smoke wire technique in the experiment, and the streamlines in the simulation are coloured by the velocity magnitude nondimensionalized by the freestream velocity. At $\alpha = \alpha_1$, one can observe that the flow is not fully attached to the upper surface of the wing, and the flow separation shows prominent three-dimensional characteristics, as shown in Fig. 6c and Fig. 6d. Namely, the streamlines near the inboard slat region defined in Fig. 4 are parallel to the flow direction. At the region where the distance between it and the inboard slat is around $0.08C$, however, a large vortex is formed. Then, the streamlines almost turn back and interact with the freestream flow.

3.2. Lift and drag coefficients

Numerical simulations and experiments are performed at various angles of attack to obtain the lift and drag behaviour of the multi-element airfoil. To ensure that simulations are converged, the lift and drag coefficients for each clean and active flow control case computed by the numerical simulation are averaged over 20 periods [23,24]. The lift and drag coefficients are shown in Fig. 7. The enhancement of the lift coefficient achieved by the active flow control is relatively small in the linear branch of the lift. However, compared with the clean cases, the

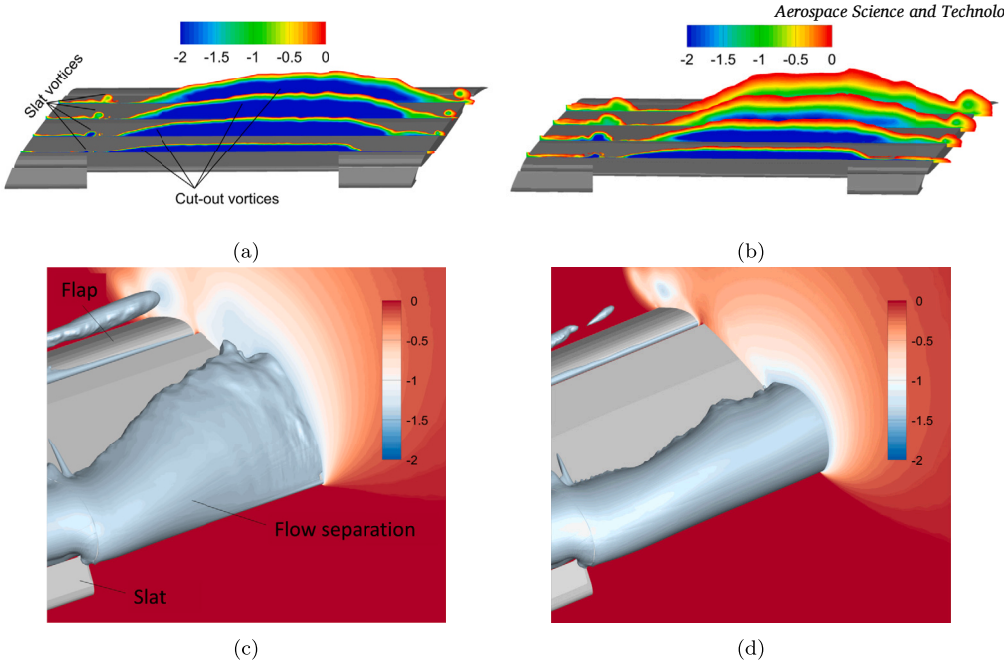

Fig. 8. Contours of total pressure coefficient C_{pt} at $\alpha = \alpha_1$ of (a) clean case and (b) active flow control case. Iso-surface of mean pressure coefficient $C_p = -1.39$ at $\alpha = \alpha_1$ of (c) clean case and (d) active flow control case.

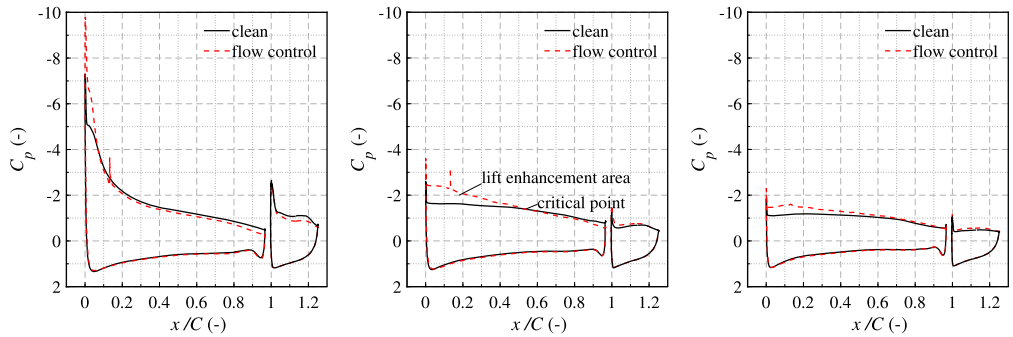

Fig. 9. Distributions of the time-averaged pressure coefficients at three cut-planes at $\alpha = \alpha_1$.

enhancements of the maximum lift coefficient are 16% and 19% for the experiment and simulation, respectively. The stall angle is significantly delayed at around 4°for the active flow control cases at a higher angle of attack. Therefore, the active flow control illustrates enhancements for the maximum lift and stall angle [44]. Additionally, resembling results of reference [23,44,45], there is a considerable gap that is small relative to the active flow control effect (the difference is less than 0.1) for the linear branch of the lift coefficients computed from experiments and simulations, as shown in Fig. 7a. Moreover, the active flow control does not have an obvious penalty on the drag coefficients at various angles of attack compared with clean cases, as shown in Fig. 7b.

3.3. Pressure coefficient

The total pressure coefficients C_{pt} are shown in Fig. 8a and Fig. 8b. The negative values represent the total pressure deficit mainly caused by the vortex system (off the surface) and near-wall viscous effects. Similar to reference [46], the slat vortex and cut-out vortex are observed. The cut-out vortex limits the growth of the low-pressure region on the main-element wing. Hence, compared with the clean case, the extent of the low-pressure domain is remarkably reduced when the active flow control is applied, as can be seen in Fig. 8c and Fig. 8d.

The time-averaged pressure coefficient distributions over the airfoil surfaces in both clean and active flow control cases are computed. To clearly show the comparison of the pressure profile, cut-planes are extracted along the spanwise direction, and the corresponding results are shown in Fig. 9. At the region near the inboard slat, the active flow control has limited impact, featuring a tiny difference between the time-averaged pressure coefficients of clean and active flow control cases, as shown in Fig. 9a. From Fig. 9b and Fig. 9c, however, it can be observed that most of the lift enhancement in the active flow control cases is obtained in the upstream section of the suction surface, close to the leading edge of the wing, as also observed in reference [47]. This area is defined as the lift enhancement area in Fig. 9b, and will be further analyzed in the following figure. Also, one can observe that the effects of the active flow control on the pressure coefficients of the pressure surface and flap of the wing are almost negligible. Moreover, it should be noted that the spike of suction/negative pressure coefficient is caused by the jet flow, as also observed in previous work [44].

To show the region where the active flow control has a positive effect on the enhancement of the lift coefficient, fifteen cut-planes are created, and distributions of the corresponding pressure coefficients are extracted. Then, the coordinates of the critical points (i.e., see Fig. 9b) defined as the position where the jet flow does not affect the lift coefficient are plotted in Fig. 10. One can observe that the lift enhancement

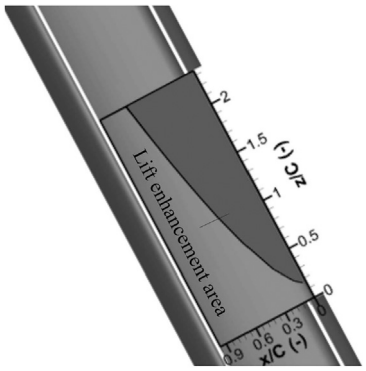

Fig. 10. Profiles of critical pressure coefficient points at $\alpha = \alpha_1$.

area close to the leading edge becomes larger along the spanwise direction. Near the inboard slat region defined in Fig. 4, the jet flow of 8 nozzles does not have significant effects on the lift coefficient.

3.4. Analysis of flow separation suppression

In addition, the numerical simulations are deployed to shed more insights into the physics of the flow around the wing. For such a swept wing, the flow separation around the wing surface is essentially a three dimensional structure with a strong spanwise velocity component. By treating the $\alpha = \alpha_1$ cases without/with active flow control as examples, the time-averaged streamlines for four cut-planes extracted along the spanwise direction are visualized in Fig. 11. For the clean case, the flow is attached to the upper surface of the wing, as shown in Fig. 11a. Resembling an observation in reference [48], the size of the leading edge vortex gradually increases along the spanwise direction, and it almost covers all the suction surface of the wing at cut-planes $z/C = 1.42$, $z/C = 1.79$ and $z/C = 2.09$ where the flow is completely separated, as can be seen from Figs. 11b to 11d. After applying the active flow control, the change in flow pattern at the cut-plane $z/C = 0.16$ shown in Fig. 11e is minimal. On the contrary, as shown in Fig. 11f, Fig. 11g and Fig. 11h, the dimensions of the vortexes are dramatically reduced, indicating that flow separation is efficiently suppressed.

By treating the case of $\alpha = \alpha_1$ without/with active flow control as an example, the time-averaged streamwise wall shear stress on the suction surface is visualized in Fig. 12. Theoretically, the flow separation region is defined as the domain where the wall shear stress is equal to zero [49]. Based on this definition, one can observe from Fig. 12a that more than half of the wing suction surface for the clean case is in reversed separated flow where the wall shear stress is less than zero. However, as shown in Fig. 12b, the reverse flow domain is efficiently narrowed by imposing the active flow control.

The mean streamwise boundary layer velocity profiles at $z/C = 1.42$ at $\alpha = \alpha_1$ are shown in Fig. 13. The distance between an observation point and the wing surface d, and the streamwise velocity U are normalized by the chord length C and the free stream velocity U_∞, respectively. For the clean case, one can observe that the near-wall velocity of the three observation points are negative values, illustrating that flow separation has occurred. However, after imposing the active flow control, the near-wall streamwise velocities at $x/C = 0.52$ and 0.72 are positive values, indicating that flow separation has been effectively suppressed.

3.5. Mechanism analysis of lift enhancement

Some localised analysis will be reviewed in this subsection to explain the evolution of the global lift coefficient. Fig. 14 exhibits the phase averaged pressure coefficient at various cut planes. To analyze the effects of the active flow control on the suppression of flow separation, five phases (namely, $t/T_{jet} = 0.6, 0.8, 1.0, 1.2, 1.4$) of a period are chosen, and the pressure coefficient is phase-averaged for more than 20 periods to obtain a steady value. For the cut-plane $z/C = 0.16$ where flow separation does not occur (see Fig. 10), the flow is almost not affected by the active flow control, which can be observed from the negligible differences among the pressure coefficient profiles with/without active flow control, as shown in Fig. 14a. Moreover, one can observe from Figs. 14b to 14d that, in terms of other cut-planes along the spanwise direction, the pressure distribution on the bottom surface of the wing is only minorly affected by the active flow control. However, the pressure of near-leading edge region of the top surface is reduced when the jet velocity is 0, which is responsible for the lift enhancement achieved by the active flow control, as presented in Fig. 7a and Fig. 10. Also, the scale of the lift enhancement region increases gradually (by treating the cut-plane $z/C = 1.42$ shown in Fig. 14b as an example, it is $0 \leq x/C \lesssim 0.47$, $0 \leq x/C \lesssim 0.61$ or $0 \leq x/C \lesssim 0.78$ at $t/T_{jet} = 0.6, 0.8, 1.0$, respectively). For the near-leading edge region, the pressure coefficient is enhanced on the suction surface when the active flow control cycle is on, which derives the associated lift enhancement towards the trailing edge of the wing (i.e., the region $0.48 \lesssim x/C \lesssim 0.9$ at $t/T_{jet} = 1.2$ in Fig. 14b). Compared with the clean case, the value of pressure reduces again when the active flow control velocity reaches 0 (i.e., $t/T_{jet} = 1.4$), resulting in an additional lift enhancement area (i.e., the domain $0 \leq x/C \lesssim 0.20$ in Fig. 14b).

To explain the aforementioned pressure reduction at $t/T_{jet} = 1.4$ presented in Fig. 14b when actuators are switched off, the streamwise velocity profiles of two points are plotted in Fig. 15. One can observe that the reverse flow velocity of the clean case is reduced, indicating the enhancement of streamwise momentum. This observation matches previous efforts [50–53], namely, flow control causes a larger entrainment of high-momentum fluid into the near-wall region, thereby controlling separation.

The phase-averaged vortex structure of the flow field combined with the pressure coefficient at the cut-plane $z/C = 1.42$ during one jet flow period is shown in Fig. 16. When the jet flow velocity $U_{jet}/U_{jet,max}$ sketched in Fig. 2 is equal to 1.0, the leading edge vortex gradually breaks down into two vortices owing to the interactions between the jet flow and main flow. A small one is near the leading edge ($0.1 \leq x/C \leq 0.2$) and a large one is at the middle section of the wing ($0.3 \leq x/C \leq 0.6$), as shown in Fig. 16a. Then, the large vortex moves towards the trailing edge and eventually diminishes. Conversely, the dimension of the small vortex maintaining almost the same position gradually increases, and this vortex becomes the new one for the next jet flow period. Such an observation is in agreement with the previous investigation [51], namely, when the dynamic actuation frequency closes to the shedding frequency of the dominant eddy, the separated shear layer is deflected towards the surface, and a vortex trail can be seen advecting along the airfoil surface. In addition, the vortex shedding phenomenon shown in Fig. 16 in an active flow control period affects pressure distribution on the top surface (see Fig. 14), further improving the lift coefficient of the wing.

4. Conclusion

In this work, an active flow control technique using 88 pulsed jet actuators mounted near the leading edge of a slat cut-out is employed to suppress flow separation. A hybrid model combining the Large-eddy Simulation (LES) and Stress-Blended Eddy Simulation (SBES) is employed to investigate the flow physics over a high-lift multi-element airfoil. The lift and drag coefficients at various angles of attack predicted by the numerical simulations and experiments are compared. A significant flow separation region is observed for the clean case without active flow control when the angle of attack approaches α_1. Both experimental and numerical results indicate that the active flow control is able to increase the maximum lift by more than 15% as well as the stall angle by around 4°. Also, the active flow control does not have an obvious penalty on the drag coefficients at various angles of

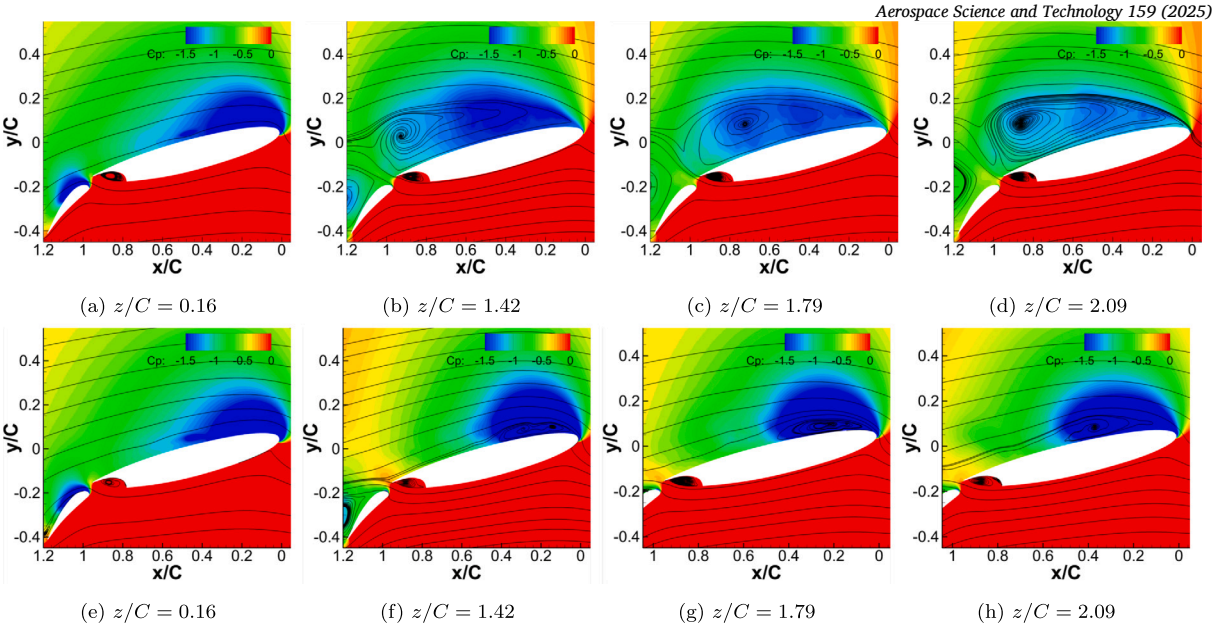

(a) $z/C = 0.16$ (b) $z/C = 1.42$ (c) $z/C = 1.79$ (d) $z/C = 2.09$

(e) $z/C = 0.16$ (f) $z/C = 1.42$ (g) $z/C = 1.79$ (h) $z/C = 2.09$

Fig. 11. Profiles of time-averaged streamline at $\alpha = \alpha_1$. The top and bottom rows of figures represent clean and active flow control cases, respectively.

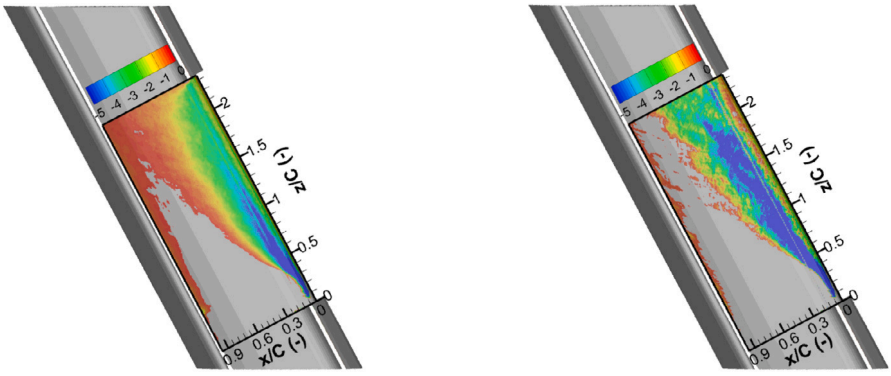

(a) Clean case (b) Active flow control case

Fig. 12. Profiles of time-averaged streamwise wall shear stress at $\alpha = \alpha_1$.

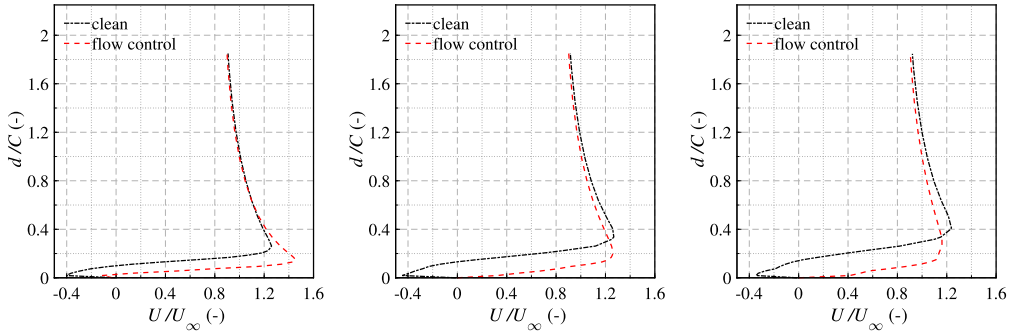

(a) $x/C = 0.32$ (b) $x/C = 0.52$ (c) $x/C = 0.72$

Fig. 13. Distributions of the mean streamwise velocity in the boundary layer at $z/C = 1.42$ and $\alpha = \alpha_1$.

attack compared with corresponding clean cases. By analyzing the pressure coefficient and visualizing the flow field, a lift enhancement area caused by the vortex shedding is formed adjacent to the leading edge when the active flow control is imposed, and its scale becomes larger along the spanwise direction. In subsequent studies, we will further investigate the effects of jet flow control across various Reynolds numbers.

CRediT authorship contribution statement

Qiangqiang Sun: Writing – review & editing, Writing – original draft, Software, Methodology, Formal analysis, Conceptualization. **Faycal Bahri:** Methodology, Data curation. **Mark Jabbal:** Writing – review & editing, Supervision, Conceptualization. **Wit Stryczniewicz:** Project administration. **Richard Jefferson-Loveday:** Writing – review

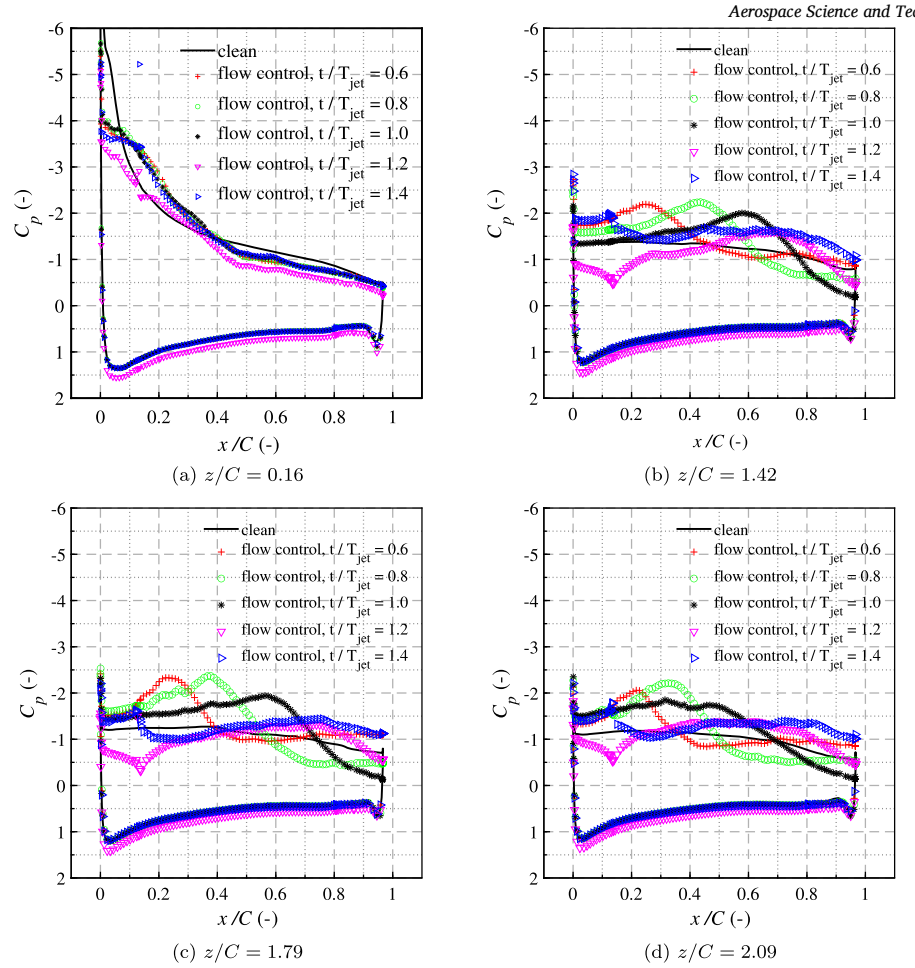

Fig. 14. Distributions of the phase averaged pressure coefficient at various cut-planes at $\alpha = \alpha_1$. The pressure coefficient of the slap is not plotted here for brevity.

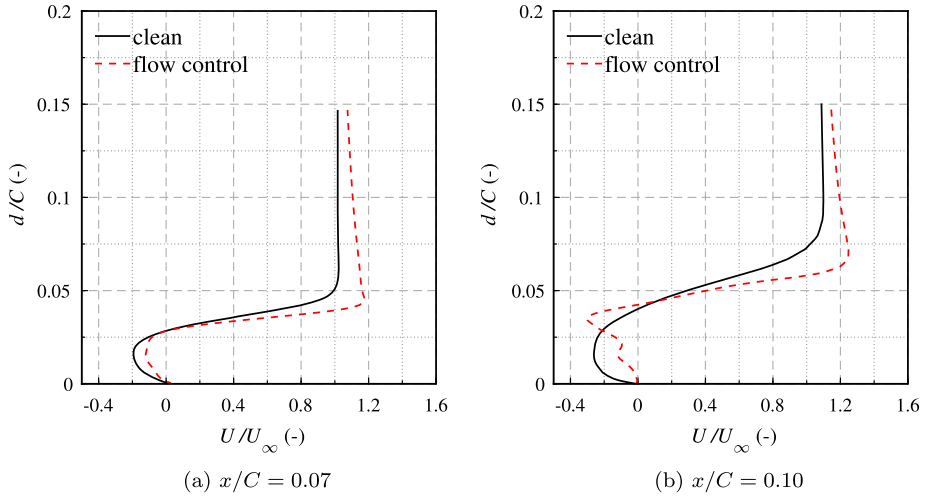

Fig. 15. Distributions of the mean (clean case) and phased-averaged (flow control case) streamwise velocities in the boundary layer at $z/C = 1.42$ and $\alpha = \alpha_1$.

& editing, Supervision, Software. **Bruno Stefes:** Project administration, Conceptualization. **Alexander Büscher:** Formal analysis, Conceptualization.

Declaration of competing interest

The authors declare that they have no known competing financial interests or personal relationships that could have appeared to influence the work reported in this paper.

Acknowledgements

This project has received funding from the Clean Sky 2 Joint Undertaking under the European Union's Horizon 2020 research and innovation programme under grant agreement No 887092 (WINGPULSE). The support of the HPC group at the University of Nottingham (AUGUSTA) and SULIS (TIER 2 HPC) is also gratefully acknowledged.

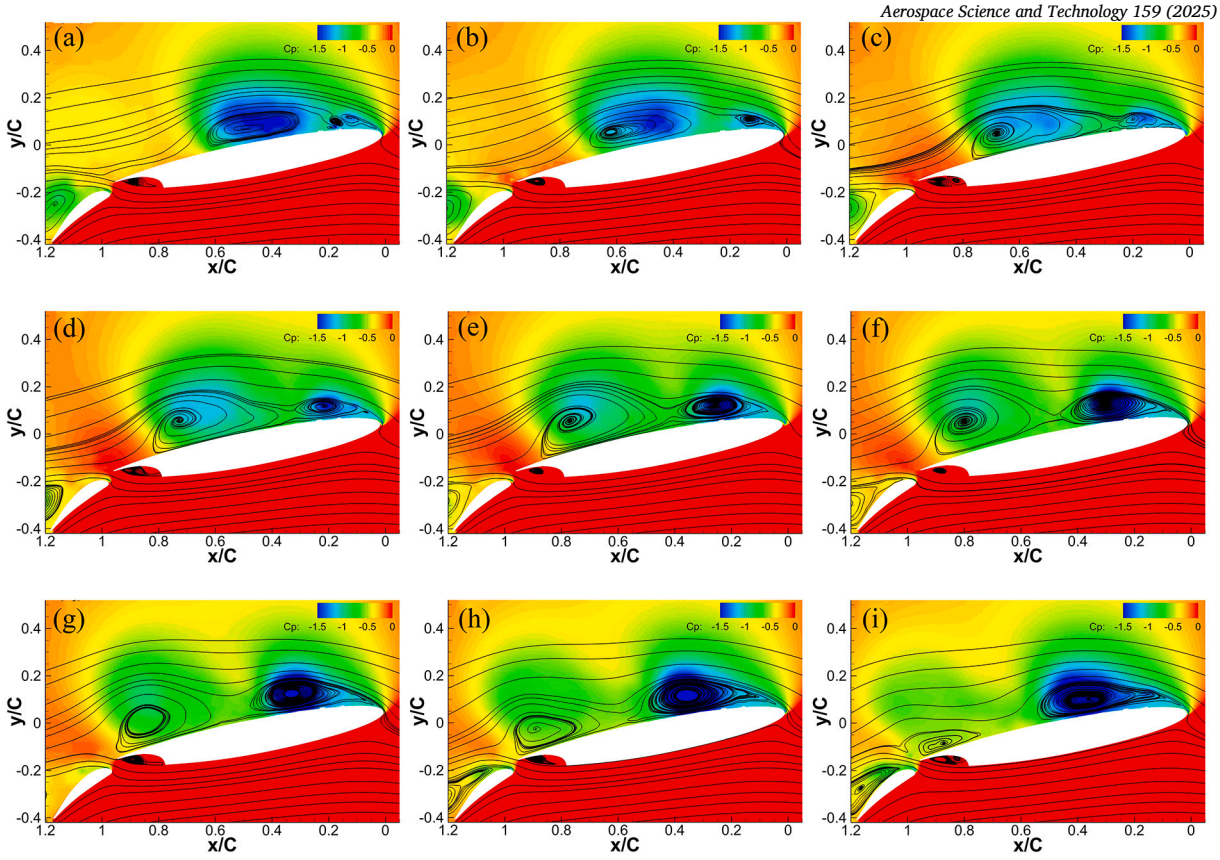

Fig. 16. Phase averaged streamlines and pressure coefficients at the cut-plane $z/C = 1.42$ in one jet flow period. (a) $t/T_c = 0.15$, (b) $t/T_c = 0.31$, (c) $t/T_c = 0.46$, (d) $t/T_c = 0.77$, (e) $t/T_c = 0.92$, (f) $t/T_c = 1.08$, (g) $t/T_c = 1.23$, (h) $t/T_c = 1.38$, (i) $t/T_c = 1.54$. $T_c = C/U_c$ is a reference time, and U_c is convective velocity. The values of $U_{jet}/U_{jet,max}$ are 1 for (a) and (b), and 0 for the others.

Data availability

Data will be made available on request.

References

[1] J. Thibert, J. Reneaux, F. Moens, J. Preist, Onera activities on high-lift devices for transport aircraft, Aeronaut. J. 99 (989) (1995) 395–411, https://doi.org/10.1017/S0001924000028700.

[2] D. Hue, C. François, J. Dandois, A. Gebhardt, Simulations of an aircraft with constant and pulsed blowing flow control at the engine/wing junction, Aerosp. Sci. Technol. 69 (2017) 659–673, https://doi.org/10.1016/j.ast.2017.07.031.

[3] S. Jiang, J. Yu, S. Yin, Y. Yang, F. Chen, P.E. Sullivan, Uncertainty quantification of separation control with synthetic jet actuator over a naca0025 airfoil, Aerosp. Sci. Technol. 133 (2023) 108106, https://doi.org/10.1016/j.ast.2023.108106.

[4] T. Kim, S. Jee, M. Kim, I. Sohn, Numerical investigation on high-speed jet actuation for transient control of flow separation, Aerosp. Sci. Technol. 135 (2023) 108171, https://doi.org/10.1016/j.ast.2023.108171.

[5] R. Sebastian, A.-M. Schreyer, Design considerations for efficient spanwise-inclined air-jet vortex generators for separation control in supersonic and hypersonic flows, Aerosp. Sci. Technol. 147 (2024) 109033, https://doi.org/10.1016/j.ast.2024.109033.

[6] A. Jirasek, Vortex-generator model and its application to flow control, J. Aircr. 42 (6) (2005) 1486–1491, https://doi.org/10.2514/1.12220.

[7] A. Glezer, M. Amitay, Synthetic jets, Annu. Rev. Fluid Mech. 34 (1) (2002) 503–529, https://doi.org/10.1146/annurev.fluid.34.090501.094913.

[8] N. Findanis, N. Ahmed, The interaction of an asymmetrical localised synthetic jet on a side-supported sphere, J. Fluids Struct. 24 (7) (2008) 1006–1020, https://doi.org/10.1016/j.jfluidstructs.2008.02.002.

[9] S. Aubrun, A. Leroy, P. Devinant, A review of wind turbine-oriented active flow control strategies, Exp. Fluids 58 (10) (2017) 1–21, https://doi.org/10.1007/s00348-017-2412-0.

[10] H. Bieler, Active flow control concepts and application opportunities, Aircr. Eng. Aerosp. Technol. (2017), https://doi.org/10.1108/AEAT-01-2017-0015.

[11] J. Ortmanns, M. Bitter, C.J. Kähler, Dynamic vortex structures for flow-control applications, Exp. Fluids 44 (3) (2008) 397–408, https://doi.org/10.1007/s00348-007-0442-8.

[12] M.G. De Giorgi, C.G. De Luca, A. Ficarella, F. Marra, Comparison between synthetic jets and continuous jets for active flow control: application on a naca 0015 and a compressor stator cascade, Aerosp. Sci. Technol. 43 (2015) 256–280, https://doi.org/10.1016/j.ast.2015.03.004.

[13] K. Xu, G. Zha, Enhancing aircraft control surface effectiveness by co-flow jet flap at low energy expenditure, Aerosp. Sci. Technol. 133 (2023) 108145, https://doi.org/10.1016/j.ast.2023.108145.

[14] F. Deng, H. Wang, C. Xue, N. Qin, A combined experimental and numerical study on aerodynamic load reduction for a swept wing by using jets, Aerosp. Sci. Technol. 130 (2022) 107935, https://doi.org/10.1016/j.ast.2022.107935.

[15] K. McManus, J. Magill, K. McManus, J. Magill, Airfoil performance enhancement using pulsed jet separation control, in: 4th Shear Flow Control Conference, 1997, https://doi.org/10.2514/6.1997-1971, 1971.

[16] A. Seifert, T. Bachar, D. Koss, M. Shepshelovich, I. Wygnanski, Oscillatory blowing: a tool to delay boundary-layer separation, AIAA J. 31 (11) (1993) 2052–2060, https://doi.org/10.2514/3.49121.

[17] A. Glezer, Some aspects of aerodynamic flow control using synthetic-jet actuation, Philos. Trans. R. Soc. A, Math. Phys. Eng. Sci. 369 (1940) (2011) 1476–1494, https://doi.org/10.1007/978-3-540-36085-8_2.

[18] D. Greenblatt, I.J. Wygnanski, The control of flow separation by periodic excitation, Prog. Aerosp. Sci. 36 (7) (2000) 487–545, https://doi.org/10.1016/S0376-0421(00)00008-7.

[19] K.B. Zaman, Effect of acoustic excitation on stalled flows over an airfoil, AIAA J. 30 (6) (1992) 1492–1499, https://doi.org/10.2514/3.11092.

[20] D. Oster, I. Wygnanski, B. Dziomba, H. Fiedler, On the effect of initial conditions on the two dimensional turbulent mixing layer, in: Structure and Mechanisms of Turbulence I: Proceedings of the Symposium on Turbulence Held at, The Technische Universitä, Berlin, August 1977, pp. 1–5, Springer, 1978, pp. 48–64.

[21] I.J. Wygnanski, R.A. Petersen, Coherent motion in excited free shear flows, AIAA J. 25 (2) (1987) 201–213, https://doi.org/10.2514/3.9610.

[22] A.M. Smith, High-lift aerodynamics, J. Aircr. 12 (6) (1975) 501–530, https://doi.org/10.2514/3.59830.

[23] J.G. Coder, H.D. Ortiz-Melendez, Transitional delayed detached-eddy simulation of multielement high-lift airfoils, J. Aircr. 56 (4) (2019) 1303–1312, https://doi.org/10.2514/1.C035161.

[24] D. You, P. Moin, Active control of flow separation over an airfoil using synthetic jets, J. Fluids Struct. 24 (8) (2008) 1349–1357, https://doi.org/10.1016/j.jfluidstructs.2008.06.017.

[25] S. Chen, T. Tu, C. Zeng, Q. Meng, Modal analysis of compressor cascades with sweeping jet actuator and pulsed jet for active flow control based on large eddy simulation, Aerosp. Sci. Technol. 131 (2022) 107997, https://doi.org/10.1016/j.ast.2022.107997.

[26] Y. Lu, Q. Sun, K.-S. Choi, X. Zhang, X. Mao, Joint effects of virtual surfaces on anti-icing and drag reduction, AIAA J. (2024) 1–10, https://doi.org/10.2514/1.J064415.

[27] C.L. Rumsey, J. Slotnick, M. Long, R. Stuever, T. Wayman, Summary of the first aiaa cfd high-lift prediction workshop, J. Aircr. 48 (6) (2011) 2068–2079, https://doi.org/10.2514/1.C031447.

[28] C.L. Rumsey, J.P. Slotnick, Overview and summary of the second aiaa high-lift prediction workshop, J. Aircr. 52 (4) (2015) 1006–1025, https://doi.org/10.2514/1.C032864.

[29] C.L. Rumsey, J.P. Slotnick, A.J. Sclafani, Overview and summary of the third aiaa high lift prediction workshop, J. Aircr. 56 (2) (2019) 621–644, https://doi.org/10.2514/1.C034940.

[30] C.L. Rumsey, S.X. Ying, Prediction of high lift: review of present cfd capability, Prog. Aerosp. Sci. 38 (2) (2002) 145–180, https://doi.org/10.1016/S0376-0421(02)00003-9.

[31] P.R. Spalart, Strategies for turbulence modelling and simulations, Int. J. Heat Fluid Flow 21 (3) (2000) 252–263, https://doi.org/10.1016/S0142-727X(00)00007-2.

[32] W. Stryczniewicz, W. Stalewski, M. Jabbal, F. Bahri, Development of pulsed jet actuator for power efficient actuation concepts testing, in: AIAA AVIATION 2022 Forum, 2022, p. 3469.

[33] R.J. Jefferson-Loveday, V. Nagabhushana Rao, J.C. Tyacke, P.G. Tucker, High-order detached eddy simulation, zonal les and urans of cavity and labyrinth seal flows, Int. J. Numer. Methods Fluids 73 (9) (2013) 830–846, https://doi.org/10.1002/fld.3826.

[34] M. Germano, U. Piomelli, P. Moin, W.H. Cabot, A dynamic subgrid-scale eddy viscosity model, Phys. Fluids A, Fluid Dyn. 3 (7) (1991) 1760–1765, https://doi.org/10.1063/1.857955.

[35] F. Menter, Stress-blended eddy simulation (sbes)—a new paradigm in hybrid rans-les modeling, in: Symposium on Hybrid RANS-LES Methods, Springer, 2016, pp. 27–37.

[36] P. Khosla, S. Rubin, A diagonally dominant second-order accurate implicit scheme, Comput. Fluids 2 (2) (1974) 207–209, https://doi.org/10.1016/0045-7930(74)90014-0.

[37] P.G. Tucker, L. Davidson, Zonal k–l based large eddy simulations, Comput. Fluids 33 (2) (2004) 267–287, https://doi.org/10.1016/S0045-7930(03)00039-2.

[38] L. Davidson, S.-H. Peng, Hybrid les-rans modelling: a one-equation sgs model combined with ak–ω model for predicting recirculating flows, Int. J. Numer. Methods Fluids 43 (9) (2003) 1003–1018, https://doi.org/10.1002/fld.512.

[39] Y. Zhang, H. Chen, K. Wang, M. Wang, Aeroacoustic prediction of a multi-element airfoil using wall-modeled large-eddy simulation, AIAA J. 55 (12) (2017) 4219–4233, https://doi.org/10.2514/1.J055853.

[40] V. Ciobaca, J. Dandois, H. Bieler, A cfd benchmark for flow separation control application, Int. J. Flow Control 6 (3) (2014), https://doi.org/10.1260/1756-8250.6.3.67.

[41] V. Togiti, B. Eisfeld, T. Knopp, et al., Numerical simulation of steady blowing active flow control using a differential Reynolds stress model, https://elib.dlr.de/60600/, 2009.

[42] R. Joslin, S. Viken, Aerodynamic performance of an active flow control configuration using unstructured-grid rans, in: 39th Aerospace Sciences Meeting and Exhibit, 2001, p. 248.

[43] J.A. Ekaterinaris, Prediction of active flow control performance on airfoils and wings, Aerosp. Sci. Technol. 8 (5) (2004) 401–410, https://doi.org/10.1016/j.ast.2004.02.003.

[44] V. Ciobaca, J. Wild, An overview of recent dlr contributions on active flow-separation control studies for high-lift configurations, Aerosp. Lab. 6 (2013) 1, https://elib.dlr.de/83559/.

[45] A. Bertelrud, J. Anders, Transition documentation on a three-element high-lift configuration at high Reynolds numbers: analysis, Tech. Rep., https://doi.org/10.2514/6.1998-703, 2002.

[46] M. Koklu, J.C. Lin, J.A. Hannon, L.P. Melton, M.Y. Andino, K.B. Paschal, V.N. Vatsa, Investigation of the nacelle/pylon vortex system on the high-lift common research model, AIAA J. 59 (9) (2021) 3748–3763, https://doi.org/10.2514/1.J059869.

[47] B.L. Ramos, W.R. Wolf, C.-A. Yeh, K. Taira, Active flow control for drag reduction of a plunging airfoil under deep dynamic stall, Phys. Rev. Fluids 4 (7) (2019) 074603, https://doi.org/10.1103/PhysRevFluids.4.074603.

[48] A.D. Gardner, K. Richter, Influence of rotation on dynamic stall, J. Am. Helicopter Soc. 58 (3) (2013) 1–9, https://doi.org/10.4050/JAHS.58.032001.

[49] R.L. Simpson, Turbulent boundary-layer separation, Annu. Rev. Fluid Mech. 21 (1) (1989) 205–232, https://doi.org/10.1146/annurev.fl.21.010189.001225.

[50] B. Steinfurth, J. Weiss, Boundary-layer control by means of pulsed jets at different inclination angles, AIAA J. 59 (10) (2021) 3946–3959, https://doi.org/10.2514/1.J060474.

[51] S.D. Goodfellow, S. Yarusevych, P.E. Sullivan, Momentum coefficient as a parameter for aerodynamic flow control with synthetic jets, AIAA J. 51 (3) (2013) 623–631, https://doi.org/10.2514/1.J051935.

[52] A. Seifert, A. Darabi, I. Wyganski, Delay of airfoil stall by periodic excitation, J. Aircr. 33 (4) (1996) 691–698, https://doi.org/10.2514/3.47003.

[53] R. Chang, F.-B. Hsiao, R.-N. Shyu, Forcing level effects of internal acoustic excitation on the improvement of airfoil performance, J. Aircr. 29 (5) (1992) 823–829, https://doi.org/10.2514/3.46252.